IDENTIFICATION OF FLAWS FROM SCATTERED ULTRASONIC FIELDS AS MEASURED AT A PLANAR SURFACE

L. Adler, K. Lewis, P. Szilas, and D. Fitting
The University of Tennessee
Knoxville, Tennessee 37916

ABSTRACT

Ultrasonic wave scattering from ellipsoidal and cylindrical cavities embedded in titanium was measured and analyzed with a newly designed signal processing system. Using an immersion system and samples with flat faces, the range for waves incident, at certain polar and azimuthal angles, was determined for both L-L and L-S scattering. Attempts were made to define key parameters from both amplitude and phase spectra for characterizing cavities. Results are compared to predictions of Born approximations (developed by Krumhansl et al. at Cornell) and to experimental results taken by a contact system (Tittmann et al. at Rockwell). A new (Keller type) theory for crack-like defects which includes mode conversion will also be presented.

Introduction

The objective of the third year was to concentrate efforts among the various investigators upon the inverse problem. In an effort to obtain size and orientation of cavities from scattering data, our specific goal was to design system and data processing to obtain optimum information for scattering data within the experimental limitations of an immersed system using flat samples. Then by taking a large number of scattering data: (a) provide Adaptronics with this data to test their adaptive technique which is trained based on Born approximations, and (b) direct comparisons of the data to available models.

Experimental Technique

In previous investigations one of two techniques was used. These are: (a) normal incidence pitch-catch method, and (b) pulse-echo at various angles. Since both of these techniques have advantages, they were utilized in combination. Figure 1 illustrates the new experimental technique used in the third year. The transmitter launches a longitudinal wave to the liquid-solid interface at an angle such that both L and S waves are generated. The cavity can be insonified either by an L wave or by an S wave. Only L waves incident to the cavity are considered, which is mode converted into L and S waves. The configuration of the receiver is shown to receive only scattered L or scattered S waves. The transmitter can also be used to receive scattered L waves (this special case is the pulse-echo technique). This arrangement has the flexibility to vary the incident angle α and the scattered polar angle θ. The coordinate system used is shown in Fig. 2. The right side of the coordinate system is attached to the sample and used as experimental parameters. On the left the coordinate system is attached to the cavity and this is used by the Born approximation theory. One set of angles can be expressed in terms of the other by using a coordinate transformation. The system was also modified to receive in different planes; i.e., for fixed incident angle α and polar angle θ we have the capability to study the dependence on azimuthal angle ϕ. The new multiplane goniometer is shown in Fig. 3. The receiver is rotated about a fixed axis while keeping the transmitter in the same plane. For each value of the incident angle α ($0°$, $10°$, $20°$, $30°$) the receiver was placed in four different planes, i.e., $\phi = -45°$, $0°$, $45°$, $90°$. In each plane the polar angle was adjusted up to $60°$. Because of the transducer's dimension, the smallest angle between transmitter and receiver was always $30°$. Altogether for L-L and L-S scattering we took approximately 120 data points for a given cavity. By reversing the transmitter and receiver or by using the pulse-echo mode, additional data points could be taken.

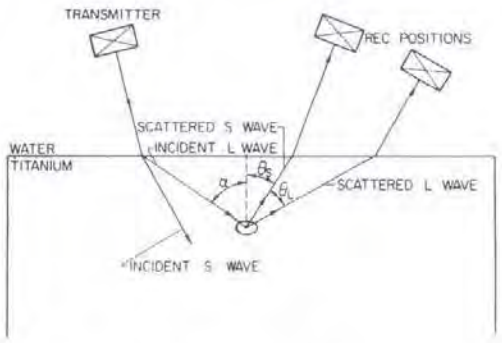

Figure 1. Experimental technique.

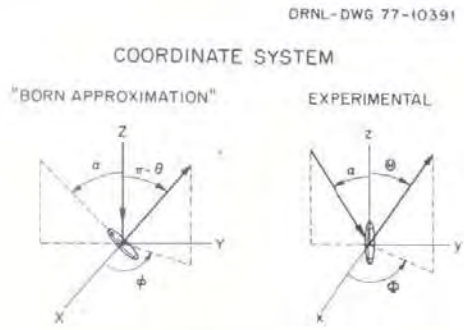

Figure 2. Coordinate system.

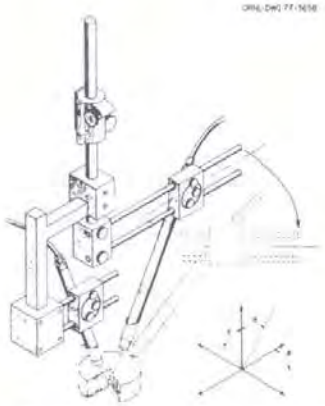

Figure 3. Multiplane ultrasonic goniometer

Modified Experimental System and Signal Processing

Our previous measurements of the frequency spectra of ultrasonic pulses were made by using a commercially available analog spectrum analyzer. This process limited out capabilities since: (1) it does not give phase information, and (2) it is not in suitable form to transfer and process the data to other investigators. Our new modified system is shown in Fig. 4. The essential feature of the system is a boxcar integrator which provides a low frequency equivalent of the rf waveform and permits digitizing the signal at an effective rate. The boxcar integrator allows one to recover and analyze signals which are far too small for data acquisition by a digitizing system. This is illustrated in Fig. 5 where the RF signal for a 40° shear wave scattered from a 200 x 400μ oblate spheroidal cavity in titanium is displayed with and without the boxcar integrator. The microprocessor is responsible for controlling the A to D converter and for conversion of the binary data to code format which is compatible with the selected peripheral device. Programs have been written which allow the data to be printed on paper tape displayed on a CRT terminal and stored on magnetic tape. The data from magnetic tape are processed by an IBM 360-91 using a FFT program. Thus one can obtain both amplitude and phase in frequency space. Figure 6 is the spectrum of a scattered wave for L-L scattering for a 500μ (diameter) disk-shaped cavity in titanium taken from the analog spectrum analyzer. The RF wave form and the processed amplitude and phase spectrum are shown in Fig. 7. In addition to phase information, the computed amplitude spectrum gives much more detail.

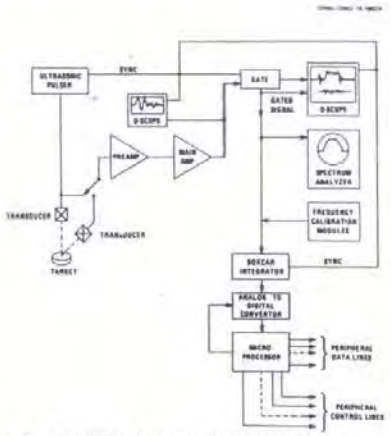

Figure 4. Modified experimental system.

(a)

(b)

Figure 5. 40° shear wave scattered from a 200 x 400μ oblate spheroidal cavity. (a) Before processing. (b) After processing.

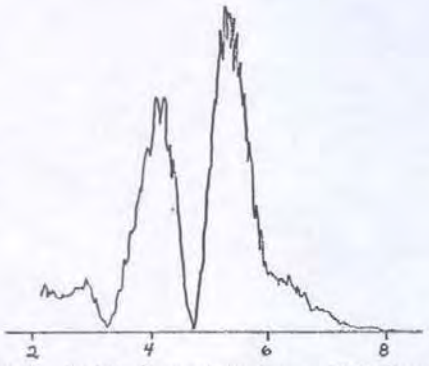

Figure 6. Amplitude spectrum from a 5000 micron disc-shaped cavity inside titanium, L-L scattering. Incident angle $\alpha = 0^\circ$; scattered angle $\theta = 60^\circ$. The spectrum is measured by the spectrum analyzer.

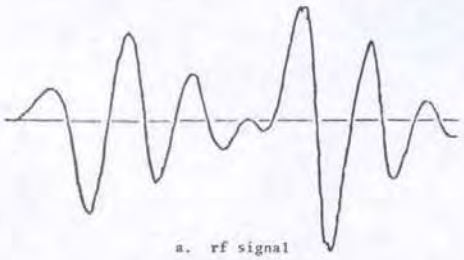

a. rf signal

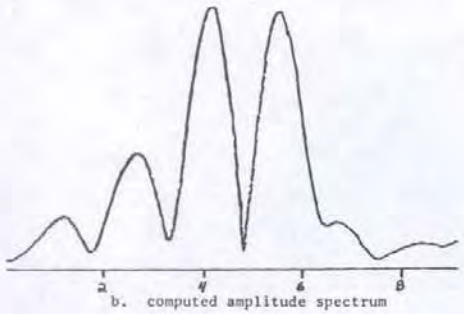

b. computed amplitude spectrum

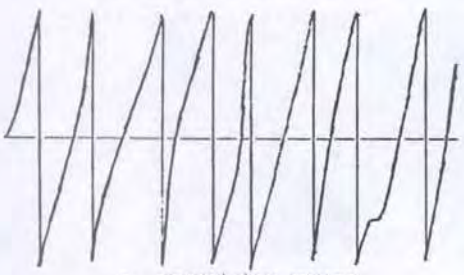

c. computed phase spectrum

Figure 7. Scattered L-L signal obtained from a 5000 micron disc-shaped cavity inside titanium. Incident angle $\alpha = 0^\circ$; scattered angle $\theta = 60^\circ$.

Correction of Data

In order to relate the experimental data to Born approximation, the data had to be corrected: (1) because of the transducer response, and (2) because of the presence of the liquid-solid interface.

Four different techniques were applied to correct for the transducer behavior shown in Fig. 8. There was very little difference in the normalizing function (transfer function) obtained in these four ways. The transmitter-receiver transfer function is shown in Fig. 9, which was taken by setting the distance between T and R to be the same as was used throughout the experiment. The amplitude (and power) data were corrected by dividing the amplitude transfer function; the phase was subtracted from the phase of the transfer function.

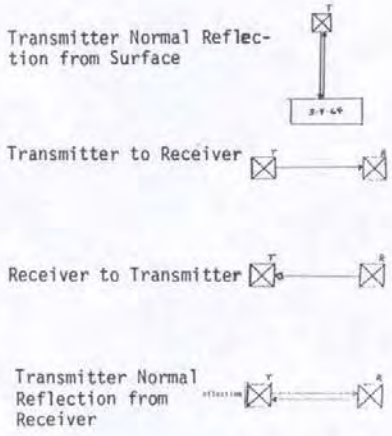

Figure 8. Normalization signals.

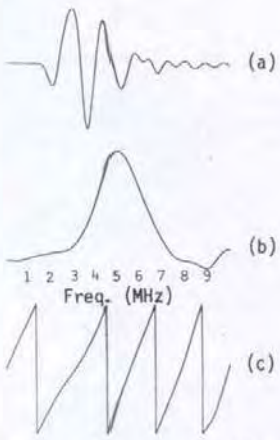

Figure 9. Transducer transfer function. (a) RF wave form; (b) amplitude spectrum; (c) phase spectrum.

The theory assumes an infinitely extended solid surrounding the cavities. The experiment, however, uses the information obtained in the liquid. The data, therefore, had to be corrected for the transmission of waves from titanium to water. In Fig. 10 the transmission amplitude vs. angle is given for L and S waves calculated by assuming infinite plane waves.

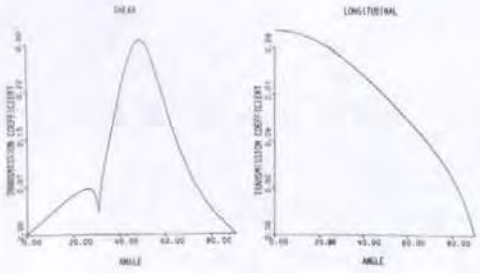

Figure 10. Transmission curve for Ti-6Al-4V water.

Procedures and Key Parameters

The different cavities used in this experiment were the following: 100 x 400μ and 200 x 400μ oblate spheroids; 200μ, 400μ, and 600μ spheres, 800 x 400μ prolate spheroid, and a 2500μ disk (the radii are given). The experimental parameters studied were the: (1) integrated power for the whole frequency region, (2) power spectra, (3) phase spectra, (4) amplitude of the center frequency, and (5) position of the center frequency. These parameters were studied for different α, θ, and ϕ for L-L and L-S scattering. The data are not complete. A complete data set is taken only on the 200 x 400μ oblate spheroid (both L-L and L-S). This was sent to Adaptronics for analyzing by their techniques of measuring size and orientation. Some data taken on the other cavities, however, are giving some understanding of the elastic wave interaction with defects.

Results

Power vs. Polar Angle Oblate Spheroid - Stereographic projection of the Born approximation, together with the experimental data, are shown in Fig. 11. For α = 0 at the center of the concentric circles, the integrated power of the pulse echo is given. Each concentric circle corresponds to a given θ and for 360° variation of ϕ. On the left the angles θ are given. The small numbers correspond to the calculated values and the larger numbers (in dB) are the measured experimental points for ϕ = 0, 45 and 90°. The drop of power with polar angle is followed by both experiment and theory. There are some uncertainties due to alignment. The data points are much better for individual frequencies. In Fig. 12 the variation of power for individual frequencies is shown. The least scatter in the data is obtained for 5.1 MHz. This is the center frequency of the input signal. There is also an increasing slope with increasing frequency.

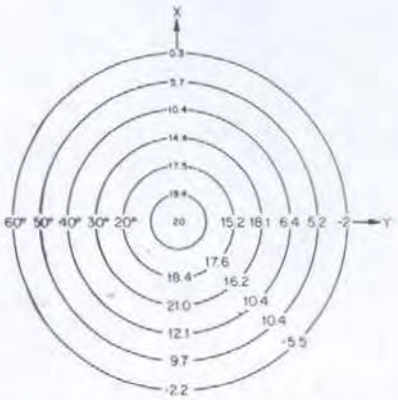

Figure 11. Stereographic projection of integrated power of L scattering for oblate spheroid α = 0. Small numbers along +X axis are calculated from Born approximation. Large numbers are measured values at ϕ = 0° (along Y) ϕ = 45° and θ = 90°.

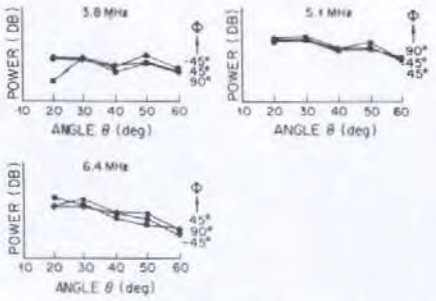

Figure 12. Scattering of longitudinal waves from a 200 x 400μ oblate spheroidal cavity in titanium, α = 0°

Scattered Field Profiles - In order to visualize some details of the predicted Born approximation we have designed a 3D plot of the scattered energy behavior based on Born approximation. In Fig. 13 the scattered power is plotted for a 200 x 400μ oblate spheroidal cavity both for L-L and L-S scattering. Here α = 0 and θ is varied from 0° to 60° and ϕ for 360°. The calculation is for a single frequency component which is 5 MHz. Now notice that from about 30° to 60° the the power falls off much faster for shear waves than for longitudinal waves (L waves and S waves

behave differently). Figure 14 shows the experimental results for the integrated power scattered from this oblate spheroid for L-L and L-S scattering. This variation from 30° to 60° is about 4 times faster for S waves than for L waves. Quantitative comparison between theory and experiment gives good results for L waves and poor results for S waves as shown in Fig. 15. The fact that ka = 2 for the L wave and 4 for the S wave gives the limitation on the Born approximation. It is significant though to point out that qualitative information can be obtained for even larger ka values from Born approximation.

Spheroid height, diameter, incident angle, minimum polar angle and frequency are:

400.0 microns, 800.0 microns, 0.0 deg., 120.0 deg., 5.1 MHz.

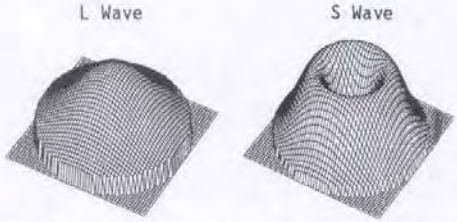

Figure 13. Calculated scattered field profile of a 5.1 MHz wave from a 400 x 800μ (diameter) oblate spheroidal cavity in titanium. $\alpha = 0°$.

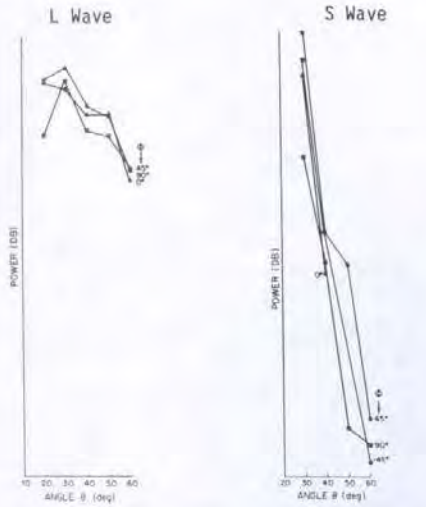

Figure 14. Integrated power vs. polar angle for scattered waves from 200 x 400μ oblate spheroidal cavity in titanium. $\alpha = 0°$.

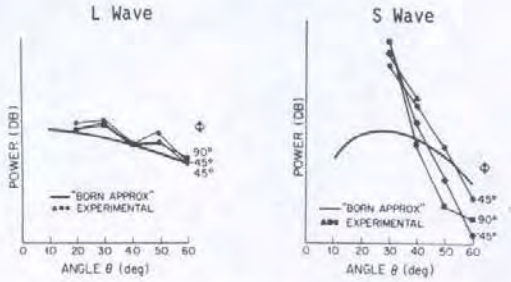

Figure 15. Power vs. polar angle for 5.1 MHz scattered waves from a 200 x 400μ oblate spheroidal cavity in titanium. $\alpha = 0°$.

Position of Peak Frequency - In Fig. 16 the position of maximum frequency is plotted vs. polar angle for L waves and for S waves scattered from a 100 x 400μ oblate spheroid. The position of the maximum frequency for L waves is unchanged, but for S waves it varies down to about 3 MHz. Born approximation again predicts this behavior, qualitatively, given by the solid lines. It may be pointed out that the variation (slope) of frequency shift is half as much for the 200 x 400μ oblate spheroid as for the 100 x 400μ oblate spheroid. This information may be used to determine size.

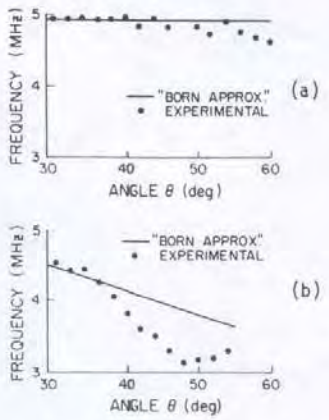

Figure 16. Maximum frequency shift as a function of polar angle for scattered (a) longitudinal and (b) shear waves from a 100 x 400μ oblate spheroidal cavity in titanium.

Normal Incidence - For non-normal incidence (or for $\alpha \neq 0$) the data for a given θ should have some φ dependence, as shown in Fig. 17, where the scattered L and S wave is given for $\alpha = 30$ for

a 200 x 400μ oblate spheroid. This information may be used to determine orientation. Experimental results are shown in Fig. 18 for $\alpha = 20°$ for a scattered S wave from an oblate spheroid. The power varies with ϕ for constant θ and varies with θ for constant ϕ. For the peak frequency, 5.1 MHz, the variation in power is shown for both L and S waves in Fig. 19 for $\alpha = 20°$, $\theta = 20°$, 30°, and 40°. It appears that the ϕ dependence agrees better with theory for S waves than the θ dependence.

Spheroid height, diameter, incident angle, minimum polar angle and frequency are:

400.0 microns, 800.0 microns, 30.0 deg., 120.0 deg., 5.0 MHz.

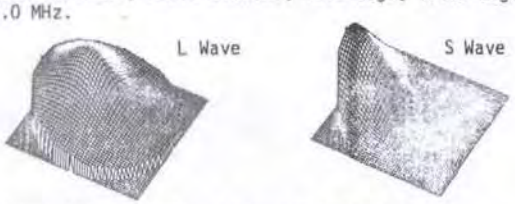

Figure 17. Calculated scattered field for non-normal incidence $\alpha = 30°$ for 400 x 800μ oblate spheroidal cavity in titanium.

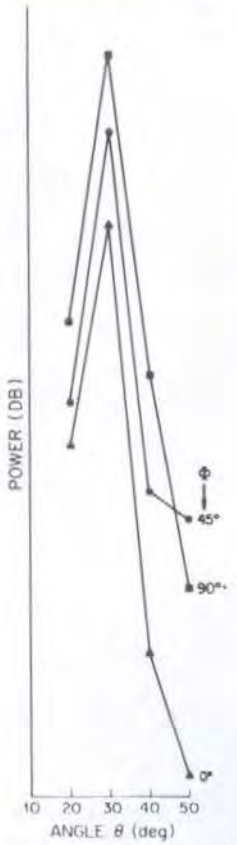

Figure 18. Integrated power vs. polar angle for S wave scattered from a 200 x 400μ oblate spheroidal cavity in titanium. $\alpha = 20°$.

Height, diameter, frequency, incident and polar angles are:

400.0 microns, 800.0 microns, 5.1 MHz, 20.0 deg., 20.0 deg.

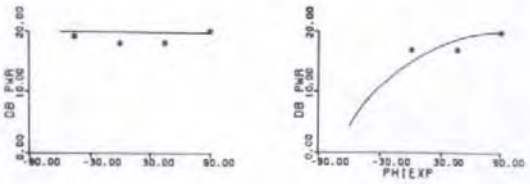

1(a) 1(b)

Height, diameter, frequency, incident and polar angles are:

400.0 microns, 800.0 microns, 5.1 MHz, 20.0 deg., 30.0 deg.

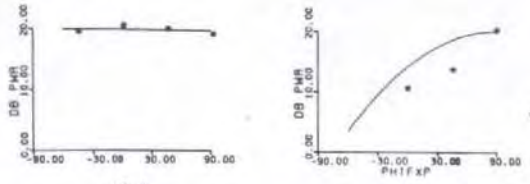

2(a) 2(b)

Height, diameter, frequency, incident and polar angles are:

400.0 microns, 800.0 microns, 5.1 MHz, 20.0 deg., 40.0 deg.

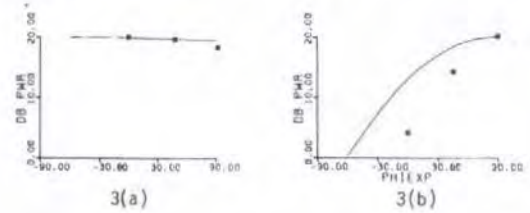

3(a) 3(b)

Figure 19. Comparison between theory and experiment for variation of scattered amplitude vs. azimuthan angle for a 400 x 800μ oblate spheroidal cavity in titanium. $\alpha = 20°$.

1. $= 20°$ (a) L wave (b) S wave
2. $= 30°$ (a) L wave (b) S wave
3. $= 40°$ (a) L wave (b) S wave

Comparison of Scattered L Field for Oblate and Prolate Spheroid - In Fig. 20 the scattered L wave and S wave for a 800 x 400μ prolate spheroid are shown for $\alpha = 0$. The behaviors are quite different than for the oblate spheroid. As we have seen before, the scattered power for an oblate spheroid decreases with increased polar angle θ, but increases for the prolate spheroid. Initial experimental results are shown in Fig. 21. For various values of ϕ the power scattered from a prolate spheroid increases with increasing polar angle. Figure 22 compares this result to the Born approximation and shows that differences in the scattered power behavior may be used for shape identification. Incidentally, this observation is in agreement with physical intuition. The oblate spheroid behaves like a piston source and the end of the prolate spheroid would behave like a point source following the observed behaviors. Further insight may be gained by taking data on L-S scattering from prolate spheroids.

Spheroid height, diameter, incident angle, minimum polar angle and frequency are:

1600.0 microns, 800.0 microns, 0.0 deg., 120.0 deg., 5.1 MHz.

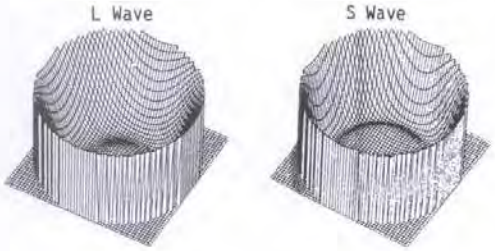

Figure 20. Calculated scattered field for 1600 x 800μ (diameter) prolate spheroidal cavities in titanium. $\alpha = 0°$.

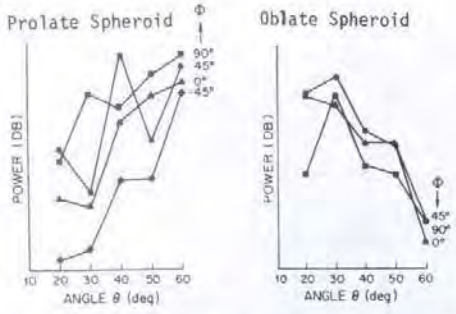

Figure 21. Integrated power vs. polar angle for L wave scattering.

200 x 400μ Oblate Spheroid

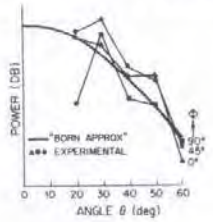

800 x 400μ Prolate Spheroid

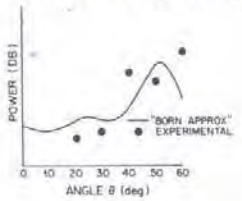

Figure 22. Integrated power vs. polar angle for scattered L waves. $\alpha = 0°$

Phase Spectra for Spherical Cavities - Not to consider phase information of a complex signal is throwing half the information away. The Born approximation does not give any phase information and the only exact theory available at the moment is for a spherical cavity.[1] We have been taking L scattering data from three different sizes of spheres to gain some insight as to what type of information is contained in the phase spectra. Our results are preliminary and far from conclusive. In Fig. 23 the phase spectra for L-L scattering is shown for $\alpha = 0$ and for three different polar angles, $\theta = 20°$, $40°$, and $60°$. It appears that for the largest sphere there is no variation of the phase spectrum with angle and for the smallest one there is variation with polar angle. We are in the process of calculating this phase spectra from the exact theory.

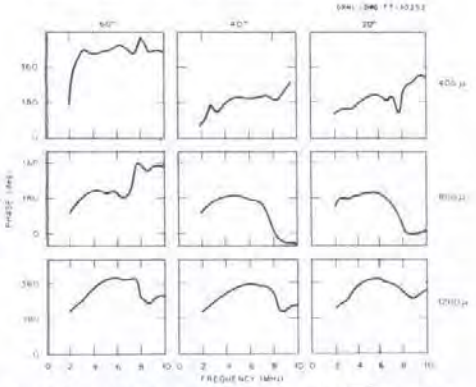

Figure 23. Phase spectra vs. polar angles for three different diameter spherical cavities in titanium.

Elastic Geometrical Theory of Diffraction for the Region ka $\geq$ 1 - As stated before, the L-L scattering for planar flaws and for ka $\geq$ 1, Keller's geometrical theory for electromagnetic waves, was successfully applied. By gaining more insight into the mode conversion problem we learned there are different types behavior from L-L and L-S scattering. We decided to tackle an elastic theory for geometrical diffraction. On the one hand, the semi-infinite plane for elastic problems was solved by Maue.[2] This result was taken and, following the concept of Keller, it was assumed that an incident L ray produces an S ray and an L ray (see Fig. 24). It is further assumed that the incident ray is proportional to the diffracted rays through D_L and D_S which are the diffraction coefficients for L waves and S waves, respectively. These diffraction coefficients are evaluated by comparing the exact solution from the half plane to a planar crack of arbitrary curvature. The solution is given in the far field. A similar procedure can be used to determine L and S diffracted fields for an incident S wave. Figure 25 gives a theoretical plot of the scattered L amplitude and phase spectrum for a 2500μ circular flaw. The dotted lines are the experimental amplitude spectrum which agrees well with theory. The calculated phase spectrum indicates that there is a sudden change in phase each time there is a minimum in the amplitude spectrum. Further experimental verification of this elastic diffraction theory is needed.

Conclusions

We have designed an experimental system which is capable of collecting a data base for quantitative flaw evaluation. The system is such that it can be used directly for a realistic NDT environment. Signal processing techniques have been applied to obtain information from scattering centers as small as 100μ in titanium--which may not be the lower limit. It has been established that both L-L and L-S scattering can be studied on an immersed system. These two types of scattering mechanisms provide useful and different information. With the same system, S-L and S-S scattering mechanisms will be studied. A data base is collected for several cavities with symmetrical geometry. Several key parameters of scattering have been identified which relate to size, orientation, and shape of the cavity such as variation of integrated power with polar angle and azimuthal angle, shift of frequency peak position with polar angle, the shape of this variation, phase spectra, etc. Direct comparison between theory and experiment establishes that the Born approximation holds well for ka < 2. On the other hand, for planar flaws and for larger ka geometrical theory of diffraction holds a lot of promise.

More experimental work and the development of a theory covering a large range of ka for crack-like flaws should be continued. Special emphasis should be placed on phase data which contain 50% of the information on scattering center.

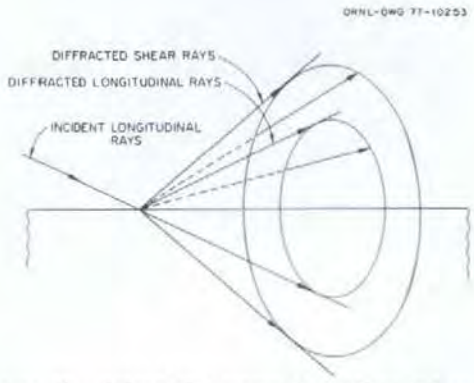

Figure 24. Schematic diagram for diffracted ray formation at an edge.

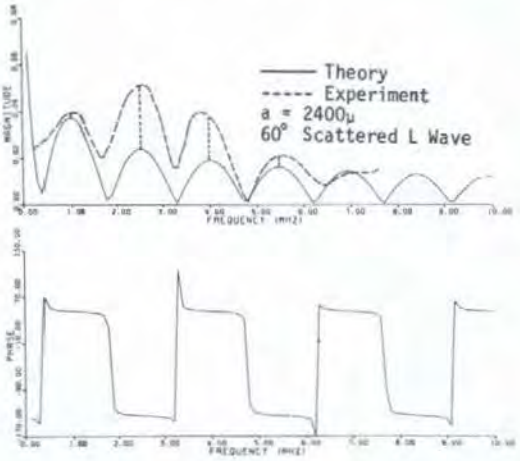

Figure 25. Plot of the scattered L amplitude and phase spectrum for a 2500μ circular flaw.

In summary, I would like to point out that in the last three years' effort the first attempt was made to supply NDT with a scientific base which can make the field a reliable quantitative tool of modern technology.

Acknowledgement

This research was sponsored by the Center for Advanced NDE operated by the Science Center, Rockwell International, for the Advanced Research Projects Agency and the Air Force Materials Laboratory under contract F33615-74-C-5180.

References

1. C. F. Ying and R. Truell, J. Appl. Phys., 27, 1086 (1956).

2. A. W. Maue, Z. Für Angew. Math. U. Mech., 33, 1 (1953).